Collimation of a D-D Neutron Generator for Clinical Implementation of Neutron Stimulated Emission Computed Tomography: a Monte Carlo Study

by

Grant Fong

Graduate Program in Medical Physics
Duke University

Date:_____

Approved:

_____
Anuj Kapadia, Supervisor

_____
Robert Reiman

_____
Timothy Turkington

Thesis submitted in partial fulfillment of
the requirements for the degree of
Master of Science in the Graduate Program
in Medical Physics in the Graduate School
of Duke University

2016

ABSTRACT

Collimation of a D-D Neutron Generator for Clinical Implementation of Neutron Stimulated Emission Computed Tomography: a Monte Carlo Study

by

Grant Fong

Graduate Program in Medical Physics
Duke University

Date:_____

Approved:

_____
Anuj Kapadia, Supervisor

_____
Robert Reiman

_____
Timothy Turkington

An abstract of a thesis submitted in partial fulfillment of the requirements for the degree of Master of Science in the Graduate Program in Medical Physics in the Graduate School of Duke University

2016

Abstract

This work is an investigation into collimator designs for a deuterium-deuterium (DD) neutron generator for an inexpensive and compact neutron imaging system that can be implemented in a hospital. The envisioned application is for a spectroscopic imaging technique called neutron stimulated emission computed tomography (NSECT).

Previous NSECT studies have been performed using a Van-de-Graaff accelerator at the Triangle Universities Nuclear Laboratory (TUNL) in Duke University. This facility has provided invaluable research into the development of NSECT. To transition the current imaging method into a clinically feasible system, there is a need for a high-intensity fast neutron source that can produce collimated beams. The DD neutron generator from Adelphi Technologies Inc. is being explored as a possible candidate to provide the uncollimated neutrons. This DD generator is a compact source that produces 2.5 MeV fast neutrons with intensities of 10^{12} n/s (4π). The neutron energy is sufficient to excite most isotopes of interest in the body with the exception of carbon and oxygen. However, a special collimator is needed to collimate the 4π neutron emission into a narrow beam. This work describes the development and evaluation of a series of collimator designs to collimate the DD generator for narrow beams suitable for NSECT imaging.

A neutron collimator made of high-density polyethylene (HDPE) and lead was modeled and simulated using the GEANT4 toolkit. The collimator was designed as a 52 x 52 x 52 cm^3 HDPE block coupled with 1 cm lead shielding. Non-tapering (cylindrical) and tapering (conical) opening designs were modeled into the collimator to permit passage of neutrons. The shape, size, and geometry of the aperture were varied to assess the effects on the collimated neutron beam. Parameters varied were: inlet diameter (1-5 cm), outlet diameter (1-5 cm), aperture diameter (0.5-1.5 cm), and aperture placement (13-39 cm). For each combination of collimator parameters, the spatial and energy distributions of neutrons and gammas were tracked and analyzed to determine three performance parameters: neutron beam-width, primary neutron flux, and the output quality. To evaluate these parameters, the simulated neutron beams are then regenerated for a NSECT breast scan. Scan involved a realistic breast lesion implanted into an anthropomorphic female phantom.

This work indicates potential for collimating and shielding a DD neutron generator for use in a clinical NSECT system. The proposed collimator designs produced a well-collimated neutron beam that can be used for NSECT breast imaging. The aperture diameter showed a strong correlation to the beam-width, where the collimated neutron beam-width was about 10% larger than the physical aperture diameter. In addition, a collimator opening consisting of a tapering inlet and cylindrical outlet allowed greater neutron throughput when compared to a simple cylindrical opening.

The tapering inlet design can allow additional neutron throughput when the neck is placed farther from the source. On the other hand, the tapering designs also decrease output quality (i.e. increase in stray neutrons outside the primary collimated beam). All collimators are cataloged in measures of beam-width, neutron flux, and output quality. For a particular NSECT application, an optimal choice should be based on the collimator specifications listed in this work.

Dedication

I would like to sincerely dedicate this work to my family and friends for all their continuous support. I could not have done this without your words of encouragement and motivation. Thank you.

Contents

List of Tables

List of Figures

Acknowledgements

I would like to thank my advisor, Dr. Anuj Kapadia, for being an exceptional mentor and role model. I would also like to thank the members of my lab group for being wonderful friends-- Manu Lakshmanan, Katie Albanese, and Robert Morris. Furthermore, I would like to give a special thank you to all past and future NSECT researchers.

1. Introduction

Neutron Stimulated Emission Computed Tomography (NSECT) is being developed as a technique to determine the elemental concentration in the human body through in vivo spectroscopic imaging. Current implementation of NSECT uses a collimated beam of high-energy neutrons to stimulate the stable nuclei of the elements within a sample. Neutrons, of sufficient energy, can inelastically scatter to excite the nuclei to higher states, which will promptly emit a series of gamma rays equal to the differences in energy states. These gamma rays have characteristic energies unique to the emitting elemental isotope and can be detected through a gamma spectrometer that acquires a multi-energy gamma spectrum. Analysis of the detected gamma spectrum provides the identities of the elements and the quantitative information on elemental concentration. Multiple gamma spectra are obtained by raster scanning the neutron beam across the sample in tomographic projections, which can be reconstructed into a tomographic image that represents the spatial distribution of each stimulated element within the body (Floyd et al. 2006). Through human body measurements of trace elements, NSECT imaging has demonstrated potential in diagnosis of diseases, such as breast cancer and iron overload in the human liver (Kapadia et al. 2008). While NSECT is being developed for medical and biological applications, a new imaging system is also being investigated to allow further advancement of NSECT in being a clinically-feasible utility.

The current NSECT imaging system is located at the Triangle Universities Nuclear Laboratory (TUNL) at Duke University in Durham, NC (Kapadia et al 2012). The imaging system utilizes a Van-de-Graff accelerator that can generate high-energy neutron beams sufficient to stimulate all biological isotopes of interest. While the system at TUNL has been an outstanding resource in the development of NSECT and has provided the underlying basis for the envisioned clinical technology, we must consider a hospital-roomed NSECT imaging system that can be safely operated in a clinical environment. To facilitate this clinical implementation, we are investigating an alternative neutron source capable of NSECT imaging and suitable for a clinical setting.

An attractive candidate for the purpose of the clinical NSECT system is the Deuterium-Deuterium (DD) neutron family of generators that are produced commercially by multiple manufacturers. A DD generator is a high-energy neutron source that uses the $d(d,n)^3He$ fusion reaction to produce an intense flux of neutrons. These neutrons are approximately 2.5 MeV in energy and sufficient to stimulate most elements in the human body with the exception of ^{12}C and ^{16}O. In addition, these generators are designed to be compact while being able to provide a high neutron flux of up to 10^{10} neutrons per second. Because of their source strength and small size, the DD generators show promise in serving as NSECT sources that can be operated within a

hospital. To utilize the DD generator, proper beam collimation is needed to yield a thin collimated neutron beam that would allow tomographic imaging.

The motivation for this work is to create a new collimator that will allow a 4π emitting DD generator to produce a narrow collimated beam suitable for clinical NSECT imaging applications. The neutron output corresponding to each collimator design will be evaluated to assess primary neutron flux, beam-width, and noise reduction. An optimal collimator design will be identified and used to demonstrate utility in NSECT breast scanning.

1.1 Proposed Neutron Collimator

The collimator materials have been chosen to be effective in both attenuating neutrons and gamma rays. For fast neutrons, the collimator should be made up of materials that maximize hydrogen content in a given volume, e.g., high-density polyethylene (HDPE). HDPE is a common hydrogenous material used for moderating neutrons, and easy to manufacture in custom shapes and sizes for the imaging system. The densely-packed hydrogen nuclei in HDPE can effectively moderate (i.e., slow down) fast neutrons into low-energy and subsequently absorb the neutrons in the medium. The resulting thermal capture by hydrogen (2223 keV) and carbon (1262 and 3684 keV), in HDPE, raises concern for the emission of high-energy gammas. These gamma photons can be blocked using lead, which is an efficient gamma attenuator due to its high density and atomic number. Lead can also be easily machined into custom sizes to

create the neutron collimator. Both HDPE and lead have also been previously used for collimation for NSECT at TUNL and will be readily available for the beginning stages of the new clinical system.

The framework for the neutron collimator is presented in Figure 1. The design of the collimator consists of a 52 x 52 x 52 cm^3 block made of HDPE. HDPE has a tenth value layer of approximately 8.3 cm for 2.5 MeV neutrons and will provide less than 0.0001% incident transmission for 52 cm thickness. Placed in front of the HDPE, a 1 cm lead sheet is coupled to the target-side face of the block to provide shielding for secondary gamma rays. A centimeter of lead was chosen as a preliminary thickness to evaluate lead-attenuation on the collimated neutron beam. The 1 cm value was selected as a starting estimate. In the future, thicker lead shielding will be investigated to reach dose and noise constraints. This work is mainly focused on producing a collimated neutron beam suitable for NSECT imaging.

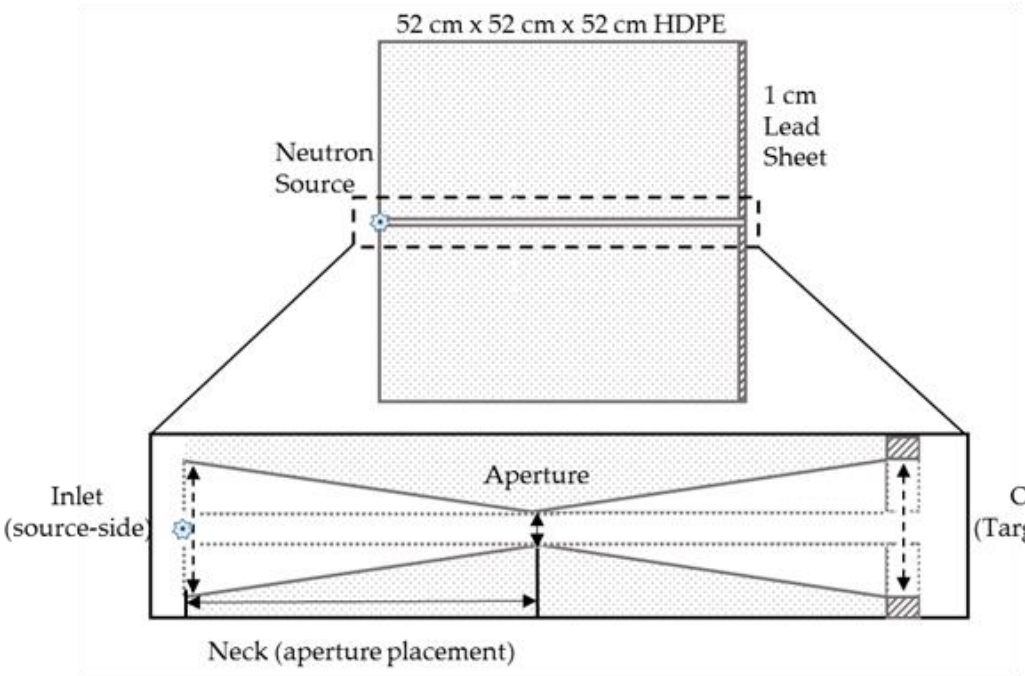

Figure 1: Geometry of DD neutron collimator being investigated. The collimator opening varies between a cylindrical design and a tapering opening based on inlet diameter, aperture diameter, outlet diameter, and neck placement.

Furthermore, the collimator consists of a central opening to allow for the passage of fast neutrons from the DD generator. This opening will be investigated and modeled by adjusting four dimensions: (1) the inlet diameter, (2) aperture diameter, (3) outlet diameter, and (4) the aperture placement, or neck, along the collimator depth. The inlet is the entryway where the DD generator is placed and the outlet is where the neutrons exit. In between the inlet and outlet, the passageway tapers down to the size of the aperture (defined as the narrowest point in the opening). Similar geometry in collimator opening has been previously used for DD generators in neutron radiography

(Barton et al. 1967). Tapering designs could have potential advantages in collimating a neutron beam for NSECT. By tapering the inlet, neutrons can scatter from the tapering wall and potentially be redirected into the primary neutron beam. The additional scattered neutrons from the tapering inlet could possibly increase collimator throughput. As for a tapering outlet, neutrons, which would have attenuated at the collimator edge, have higher probability of entering the primary beam and thereby improving neutron throughput. Both tapering inlets and outlets are expected to improve neutron throughput. An aperture, i.e., the narrowest portion of the opening, would collimate the neutrons into a narrow beam. In the investigation of the design, different diameters of the inlet, aperture, and outlet will be studied to evaluate the resulting neutron output and throughput of the collimator. In addition, the placement of the aperture will be inspected by moving the neck closer or farther from the DD generator.

In contrast to the tapering openings, the collimator of the current TUNL imaging system uses a non-tapering bore opening. The simple TUNL collimator design is already expected to produce a usable collimated beam for NSECT. However, the tapering designs are expected to have a greater neutron throughput than the cylindrical opening, which would allow NSECT imaging to reduce scan time and improve the overall efficiency in DD generator usage. To understand the benefits and drawbacks in tapering openings, a cylindrical (non-tapering) opening needs to be compared to tapering designs. Qualities reported include beam-width, noise level, and neutron flux of the

collimated output. The investigation into this series of new collimators, both tapering and cylindrical, will be cataloged for NSECT usage. The future NSECT system will have to consider the most optimal design based on the desired collimated neutron output and application.

2. Methods

The DD neutron collimators and their use in NSECT imaging were simulated and tested using the GEANT4 simulation toolkit (Agostinelli et al. 2003). GEANT4 is a highly validated open source Monte-Carlo toolkit that has been used for prior neutron imaging and benchmarking studies in our group (Lakshmanan et al. 2012, 2014). The simulations were distributed on a Duke University computer cluster with over 1200 nodes (Harrawood et al. 2014).

2.1 Experimental Set-Up

Simulation of the neutron collimators can be described in three parts as shown in Figure 2: (1) a DD neutron source, (2) neutron collimator, and (3) the detection (i.e., tracking) of particles. First, the neutron source was modeled after the DD neutron generator manufactured by Adelphi Technologies (Fuller et al 2013). Adelphi generators have a small "focal" spot where the fusion reaction and the neutron emission occur in a region smaller than 2mm. In addition, the emitted neutron spectrum is isotropic and mono-energetic of about 2.5 MeV in energy. Because of these features, the modeled neutron source was simplified to a 2.5 MeV isotropic-emission point source placed centrally at the inlet. For simulation efficiency, neutrons were only generated in the 2π direction on the collimator side. The emitted neutrons would interact with the collimator and the resulting beam properties are measured on the target side. The output of all particles spatially exiting from the target-face of the collimator is tracked to evaluate

beam properties. Energy and location of the particles were measured and binned in units of keV and millimeters, respectively. A distance of 20 cm from the collimator is being considered for being the source-to-target distance for imaging and was used to analyze most output comparison.

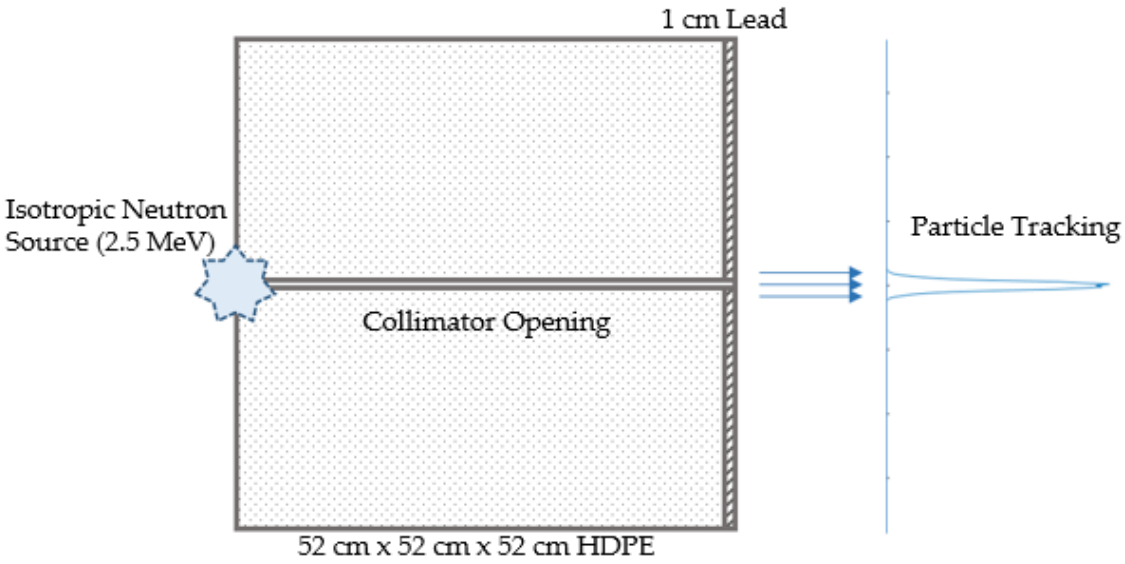

Figure 2: Monte Carlo simulation in collimating DD neutrons. Neutrons are emitted from the source and detected on the target-side.

The geometry specified for GEANT4 was modeled after the specifications of the DD neutron collimator—consisting of a 52 x 52 x 52 cm^3 cube made of HDPE with a 1-cm-thick lead sheet. The material composition used for the collimator is listed in Table 1. Density and composition were obtained from the NIST reference in the GEANT4 material database, where lead, air, and polyethylene were referred to as G4_Pb, G4_AIR, and G4_POLYETHYLENE, respectively. Their element composition contains the

elemental isotopes in their naturally occurring abundance. In addition, for each simulation, a different opening design was modeled into the collimator based on a combination of the four input variables: inlet diameter, aperture diameter, outlet diameter, and aperture placement. Using combinations of the four variables, 71 unique collimator designs were simulated. Each design was tested with 10^9 neutron histories. These simulations were used to evaluate two key physical features of the collimator: the lead shield and the collimator opening.

Table 1: Material composition in GEANT4 simulation.

Material	Density (g/cm^3)	Composition (mass fraction)
Polyethylene	0.940	C (66.67 %) H (14.37 %)
Lead	11.350	Pb (100.00%)
Air	0.00129	C (0.012 %) N (75.53 %) O (23.18 %) Ar (1.28 %)

2.1.1 Simulation Set 1: Lead Shield

Three simulations were used to investigate the lead design for the ability to preserve the collimated neutron beam and shield unwanted gamma rays. Figure 3 displays the different geometries in collimator designs. Simulations were performed

with a 1 cm cylindrical opening in the HDPE. The target-side faces are modeled with (1) no lead shield, (2) a lead shield that opens continually with the outlet, (3) and a solid lead shield that obstructed the collimator opening. Having no lead would be the least optimal collimator design because the collimator would lack an effective gamma shield. A solid lead sheet (i.e., one that blocks the opening) would attenuate the neutron beam and decrease flux. By having an opening in the lead, the design was expected to minimize neutron attenuation in the lead while acting as an effective gamma shield. The most optimal target-side face design will be used for the next simulation set.

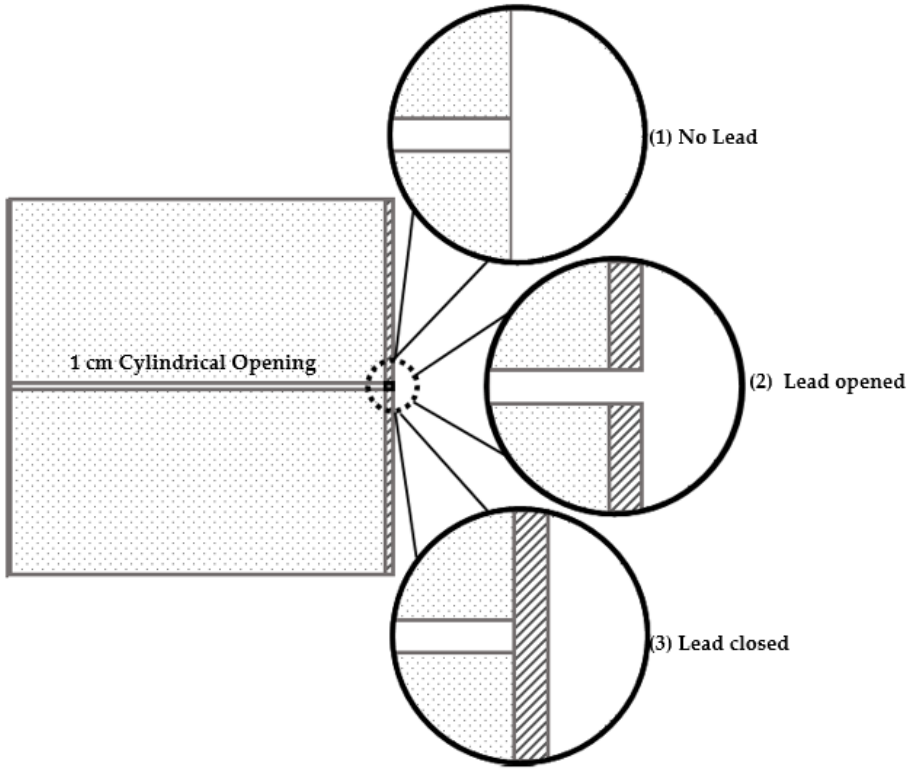

Figure 3: Three configurations of the collimator with different lead shielding – (1) No lead, (2) Lead shield with opening, and (3) Solid lead shield.

2.1.2 Simulation Set 2: Collimator Opening

The second set of Monte Carlo simulations is the series with varying inlet, outlet, and aperture sizes for the collimator. Simulations consisted of combinations in the diameter of the inlet, aperture, and outlet. These size combinations were also modeled at various aperture placements. The opening sizes and aperture placements are set to dimensions listed in Table 2. The HDPE-lead designs consisted of a lead sheet opening, where the diameter of the lead opening is set equal to the diameter of the HDPE outlet. In addition, a cylindrical non-tapering bore is modeled when the inlet and outlet openings equal the 'aperture size'.

Table 2: Dimensions investigated in tapering collimator opening.

Opening Parameters	Magnitude (cm)
Inlet: Diameter	Aperture size; and 2, 3, 4, 5 cm
Aperture: Diameter	0.5, 0.75, 1.0, 1.25, 1.5 cm
Outlet: Diameter	Aperture size; and 2, 3, 4, 5 cm
Aperture placement: Distance	13, 26, 39 cm

2.2 Beam Acquisition

Neutrons exiting the different collimator designs must be closely compared and analyzed for the purpose of evaluating the clinical NSECT system. The resulting neutron beam must be spatially well-defined and provide enough intensity for fast efficient imaging. To measure the simulated beam, a series of virtual detector planes were placed in the target area to record and bin each neutron based on its energy and point-of-incidence on the detector. These detectors have a cross-sectional area of 52 x 52 cm^2 that is perpendicular to the beam's eye view. Since the beam is expected to be narrow and well-collimated, a 52 x 52 cm^2 area provides sufficient coverage to analyze the entire beam (including divergence). These detectors are placed at increments of 5 cm, up to 50 cm, in distance from the exit face of the collimator. The particles detected at the plane provide a 52 x 52 cm^2 spatial hit map of all fast neutrons counted from 10^9 histories. This spatial hit map provides the exact coordinates of each detected particle and will be used later to regenerate a neutron beam for NSECT breast imaging. To analyze the map in terms of quality in neutron beam, a two-dimensional histogram was generated to bin the fast neutrons by location on the hit map in units of mm^2.

The detection of neutrons was discriminated by location to quantify the neutron flux occurring in the primary beam and the beam tails. A line profile through the histogram map was done to display the beam profile and determine the neutron beam-width as illustrated in Figure 4. In the beam profile, the beam-width was assumed to be

the full-width at half-maximum (FWHM). The FWHM is defined as the width of the peak at half of the maximum and will be used as the sample spacing distance for the tomographic geometry in NSECT imaging. The FWHM discriminates the neutrons as being inside or outside the beam. Particles within the FWHM are considered part of the primary beam that can effectively stimulate the area of interest. Neutrons outside the FWHM area are considered the tails of the neutron beam. Neutrons in the tails will likely excite a target volume outside the region of interest and thereby stimulating gamma emission from this unwanted region. It is possible to use larger "beam-width" discriminator such as full-width at tenth maximum (FWTM) to categorize more of the beam tail distribution as part of the primary beam. More importantly, the sample spacing distances, of either FWHM or FWTM, should be considered in tomographic imaging. Assuming a Gaussian distribution, FWTM spacing is larger than FWHM spacing, which affects the spatial resolution in the clinical NSECT system. Thus, the neutron categorization was determined by only the FWHM to allow closer sample spacing during the NSECT tomographic breast imaging described later.

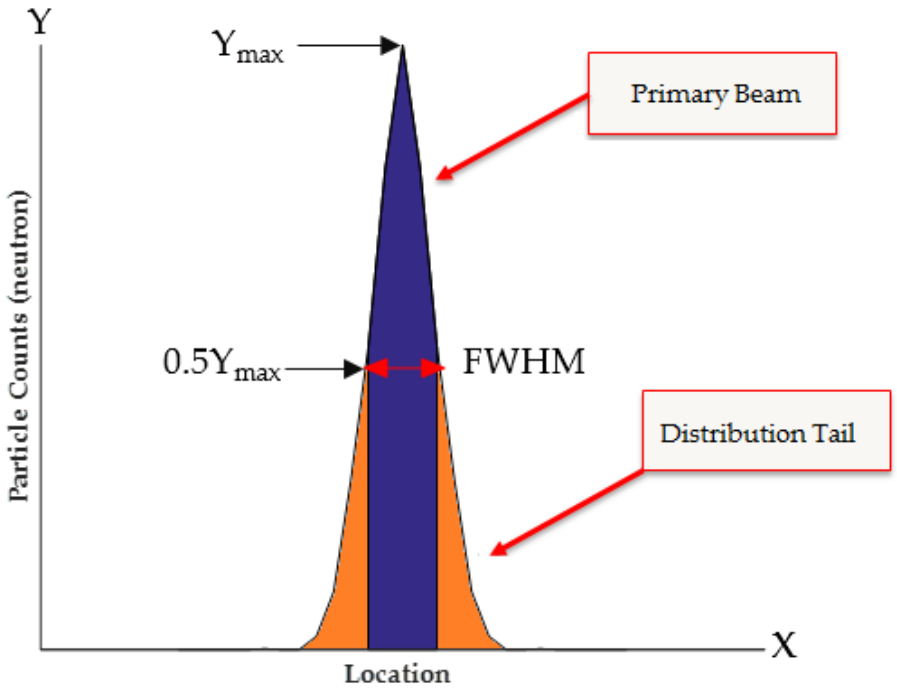

Figure 4: Neutrons are categorized as part of the primary beam or the distribution tails. The particles are discriminated by location defined by the FWHM.

Two qualities were used to analyze the resultant neutron histogram map: (1) the total beam count and (2) the output quality. The total beam count was determined by summing all fast neutrons within the FWHM beam spot. Based on 10^9 histories, the total neutrons detected in the beam spot were used to analyze throughput efficiency and scan time of the NSECT system. In addition, an output quality was introduced to quantify the usable fraction of neutrons as shown in equation 1, where N is the number of neutrons counted by the 52 x 52 cm^2 detector, *primary* indicates that the neutron counted contributes to the primary beam and *total* indicates the sum of all neutron counts

including the primary beam and tails. The output quality is the fraction of neutrons detected inside the beam to the total neutrons detected in the 52 x 52 cm^2 hits map. An output quality near 100% represents a collimated output with a majority neutron fraction in the beam while a lower output quality represents a larger fraction of neutrons is in the tails.

$$\text{Output Quality} = \frac{N_{primary}}{N_{total}} \quad (1)$$

2.3 Image Reconstruction

Select DD-neutron collimators were used to image a female breast model to detect a malignant breast lesion. Figure 5 shows the breast lesion and the anthropomorphic female phantom used for the breast scan. The lesions came from mathematically-generated models based on segmentations of high-resolution tomosynthesis images (Solomon and Samei 2014). The anthropomorphic female phantom was constructed using the XCAT program (Segars et al. 2010). The lesion was inserted near the lateral portion of the left breast. Tomographic projections were centrally taken on the left breast at an angle of 25 degrees from the coronal plane. This tomographic scan mimics the angle similar to a MLO image from mammography to avoid irradiating the heart and right breast. However, unlike mammography, the breast

of the patient is not compressed. In the envisioned clinical NSECT system, the patient would lay prone without needing any compression.

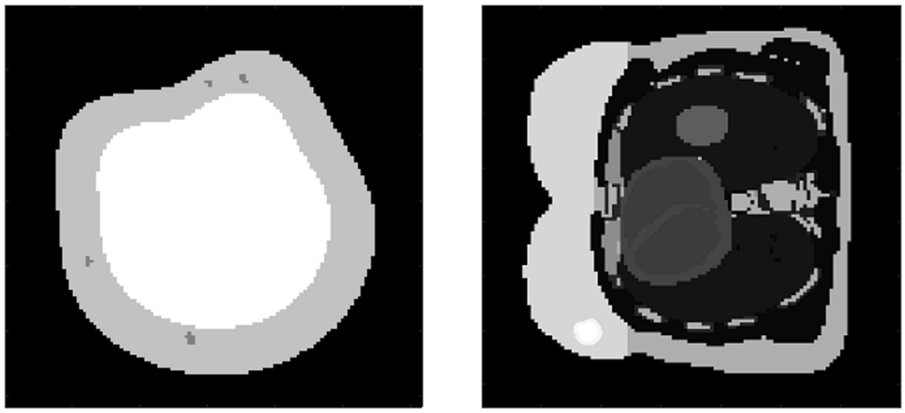

(a) Breast Lesion (b) Implant Lesion (Transverse)

(c) Implant Lesion (Coronal) (d) Implant Lesion (Sagittal)

Figure 5: Subfigure (a) shows the mathematically generated realistic breast cancer lesion with about 2.5 cm in diameter. The lesion is inserted in an anthropomorphic female phantom shown in subfigures (b-d). It can be seen in the lateral region of the left breast in the highest intensity pixel (white).

A breast scan was chosen to test the DD neutron collimators because NSECT has previously shown the feasibility in detecting breast cancer (Kapadia et al. 2008a) and the discerning ability for malignancy in breast tissues (Bender et al. 2007). Element concentrations from these studies were used to simulate the healthy and malignant breast tissues in the simulated breast scan. Element compositions are shown in Table 3. Because of the spatial resolution limitation in NSECT, the lesion was assumed homogenous with malignant concentration. Surrounding breast tissues were generated as normal concentration.

Table 3: Elemental Composition in Breast Tissue.

Element	*Normal (%)*	*Malignant (%)*
H	12.65	12.51
O	61.42	61.43
C	22.86	22.86
N	2.57	2.57
Al	6.67E-4	5.7E-4
Br	7.07E-4	6.55E-4
Ca	8.29E-3	1.13E-2
Cl	1.96E-1	2.15E-1
Co	2.06E-5	1.98E-5
Cs	3.27E-7	3.6E-7
Fe	9.80E-3	7.85E-3
K	8.94E-2	1.96E-1
Mn	3.88E-5	3.16E-5
Na	1.85E-1	2.0E-2
Rb	5.98E-4	5.84E-4
Zn	1.17E-3	1.14E-3

The spatial hit map from the collimator simulations provided neutrons at exact energy and location when detected. As the phantom is translated and rotated for tomographic imaging, the neutrons are regenerated to scan the left breast. One regenerated collimated beam output is estimated to be a 2-second beam pulse by assuming a 1 x 10^9 neutron per second intensity DD generator for the 10^9-history simulations. With this timing information, the scan-time was kept constant for all collimator designs used. However, the flux in collimated neutron beams will differ.

Once the breast model is scanned, an NSECT reconstruction algorithm was applied to the sinogram corresponding to the energy bin emitted from an element of interest (Lakshmanan et al. 2012). The energy-specific sinogram was reconstructed through a filtered back-projection followed by the Maximum Likelihood-Expectation Maximization (ML-EM) algorithm. The ML-EM algorithm (Lange and Carson 1984) performed in NSECT imaging is displayed in equation 2, where λ_j^n is the estimated pixel intensity at the *j*th pixel and *n*th iteration in the reconstructed image, *cij* is the probability matrix that a gamma ray is detected from the *j*th pixel and *i*th projection bin, *Yi* is the number of gamma rays detected for the *i*th projection, *nbin* is number of projection bins, and *nvox* is the number of pixels.

$$\lambda_j^{n+1} = \frac{\lambda_j^n}{\sum_{i=1}^{nbin} c_{ij}} \sum_{i=1}^{nbin} \frac{c_{ij} Y_i}{\sum_{k=1}^{nvox} c_{ik} \lambda_k^n} \qquad (2)$$

3. Lead Shield

Attaching a lead sheet onto the target-face of HDPE can provide shielding for unwanted secondary gammas. These gammas can interact with the patient and the imaging system. For NSECT to be clinically feasible, the radiation dose to the patient (from both neutrons and gamma rays) must be minimized. The HDPE-stimulated gamma rays can also be directly detected by detectors of imaging system, which will increase the background noise in the resulting NSECT images. The following simulations were performed to analyze the effectiveness in gamma shielding as well as preserving the primary neutron beam.

3.1 Lead Impact on Neutron Output

The addition of lead shielding into the neutron collimator must preserve the primary neutron beam with minimal interaction. The neutron beam was tracked and tallied as a function of distance from the target-side face of the collimator. Figure 6 shows the total count from the primary neutron beam detected from 5 to 50 cm. The output from the collimator design with no lead provided the baseline output of a 1 cm cylindrical opening. Total fast-neutron count for neutrons detected at 20 cm was about 1.4×10^5. In contrast, adding the lead sheet in obstruction of the collimator opening provided maximum attenuation and reduced the total neutron count to 1.1×10^5 fast neutrons (a decrease of approximately 20%). With a lead opening in the sheet, the simulation resulted in a closely comparable neutron count as without lead shielding, 1.4

x 10^5 fast neutrons. Thus, the neutron beam was minimally affected due to the lead shield design with an opening.

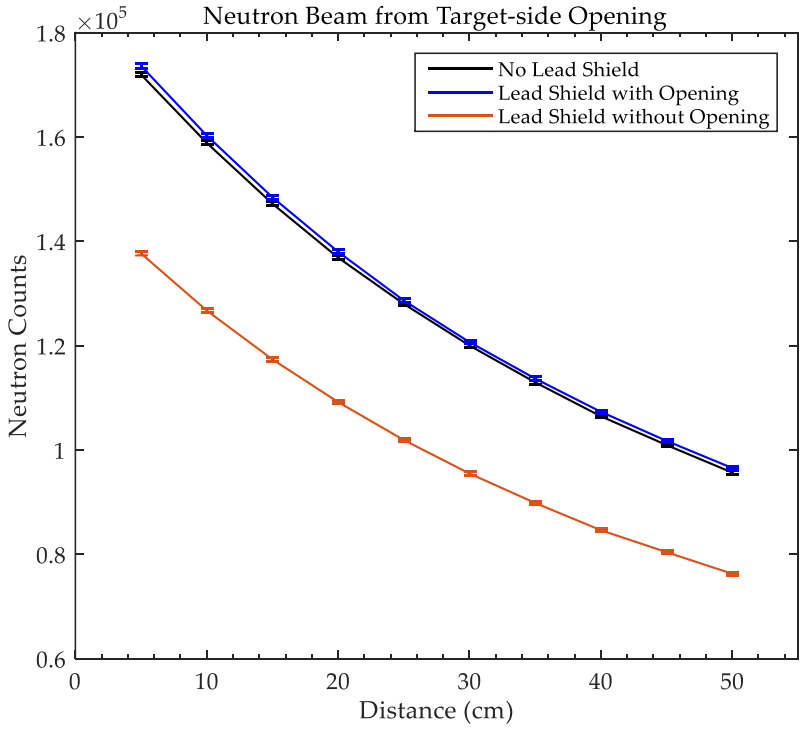

Figure 6: Comparison of neutron output with and without lead shielding in the DD neutron collimator. The opening in the lead preserves the beam flux to a magnitude comparable to having no lead.

3.2 Lead Impact on Gamma Output

The lead plate was introduced to investigate the possibility of removing secondary gamma rays using an HDPE-lead collimator design. Figure 7 displays the gamma spectra result from the three collimator simulations at 20 cm distance. Three photopeaks appear in the gamma spectra from all three simulations. Two of the

photopeaks resulted from the thermal capture emissions of neutrons by hydrogen (2224 keV) and carbon (1262 keV). The 3684 keV photon from carbon thermal capture was not displayed due to its significantly low occurrence. Another photopeak occurred at 511 keV due to the pair production of high energy photons in lead and subsequent positron annihilation that emits two 511 keV photons. Comparing these photopeaks, the most prominent gammas came from hydrogen with 2224 keV energy. The Compton scattering of the 2224 keV gammas resulted in the continuous spectrum of photons less than 2224 keV.

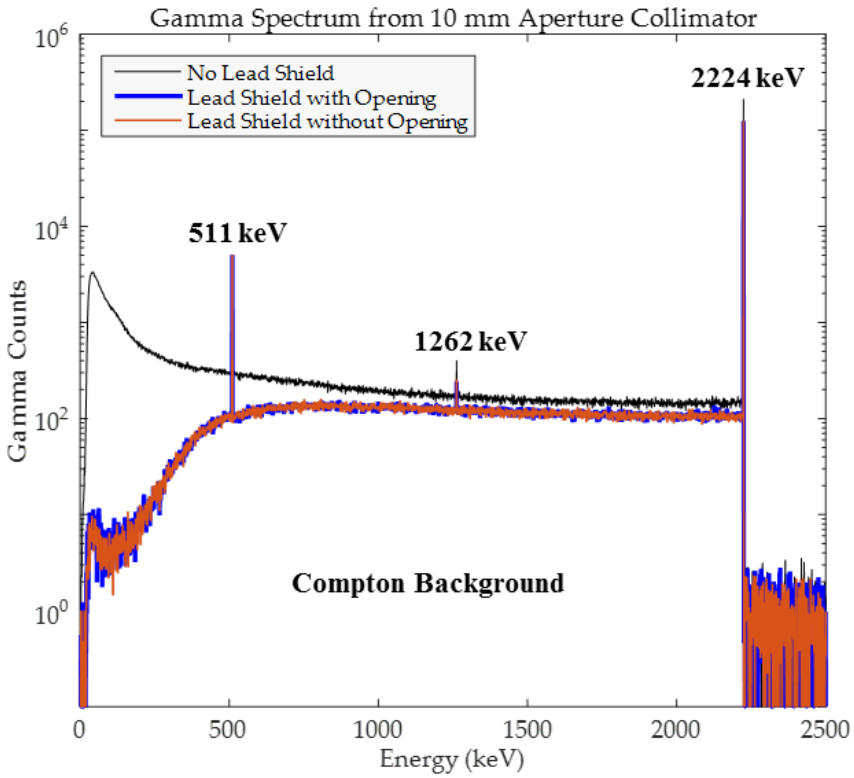

Figure 7: Gamma spectra resulting from the addition of 1 cm lead shield. The lead shield was only effective for lower energy gammas.

The addition of 1 cm lead can effectively shield lower energy photons, as expected, due to its high atomic number material. Gamma energies, up to 200 keV, decreased to about 1% or less. Thereafter, the 1 cm lead shows to be least effective as energy increases where the reaction of photoelectric absorption becomes less prominent. In addition, there was about a two-fold increase in 511 keV photons due to presence of lead. High energy photon in the presence of high atomic number mediums increases the chances of pair production which leads to a positron annihilation and two 511 keV photons. In summary, while a centimeter of lead can readily shield low energy photons, more photon shield needs to be considered for the higher energy photons.

4. Composite Collimator Opening

A series of neutron collimator simulations were performed using various designs in the collimator opening. Features were varied in the diameter of the inlet opening (2-5 cm), aperture (0.5-1.5 cm), and outlet opening (2-5 cm). The aperture location was varied at 13, 26, and 39 cm from the source-side face. Resultant neutron and gamma output were then tracked by energy and location.

4.1 Source-side vs Target-side Openings

A set of 9 simulations was first investigated for the improvement on neutron throughput by either increasing the diameter of the inlet or outlet openings. Starting with a cylindrical opening of 1cm, the inlet increased in diameter for each simulation (2, 3, 4, 5 cm) while keeping outlet constant at 1 cm. Simulations were also performed for increasing outlet diameter (2, 3, 4, 5 cm) while keeping a 1 cm inlet. The openings tapered toward the aperture, which was placed at the midpoint of the collimator (26 cm). The simulations compared the influence of a tapering inlet to a tapering outlet for the purpose of NSECT.

The total beam count is compared for the inlet and outlet designs in Figure 8. Relative to the 1 cm cylindrical opening, neutron throughput increases as the inlet diameter becomes larger. Less attenuating material and the tapered geometry permitted more throughput in fast neutrons. While keeping the source-side opening constant at 1

cm, the increase in target-side diameter did not increase the primary neutron beam significantly despite having less attenuating material.

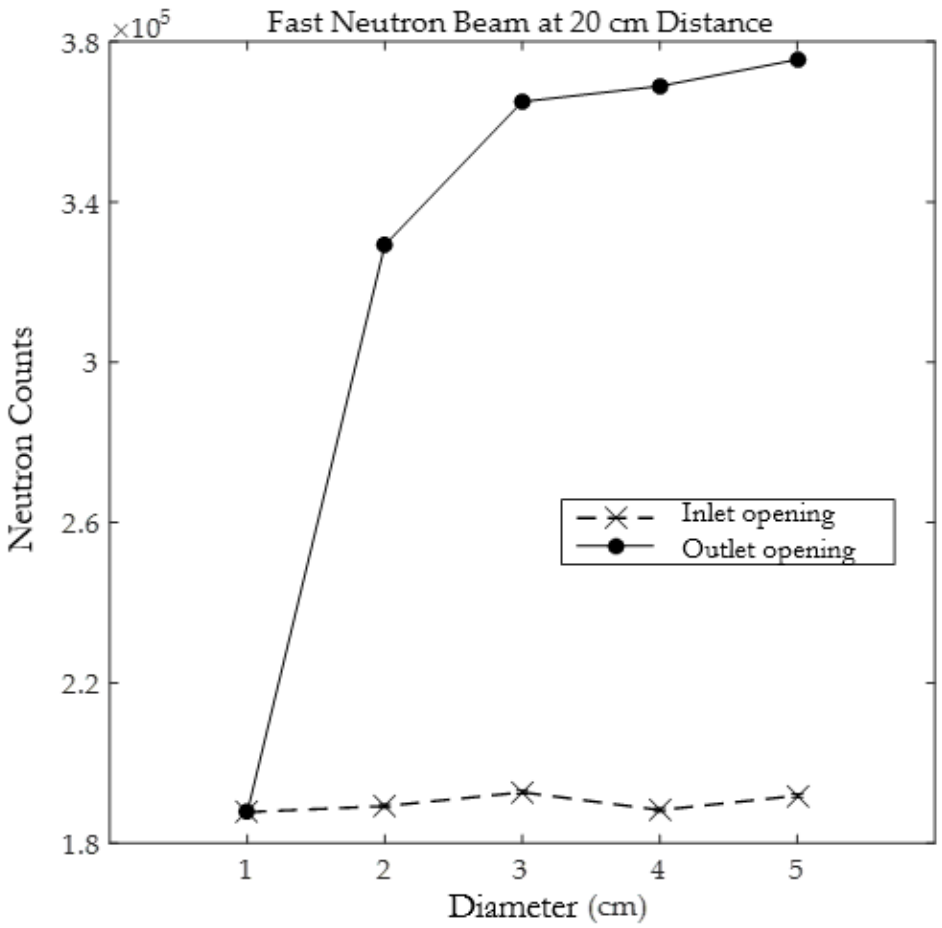

Figure 8: Comparison of primary neutron counts of collimators that varied in inlet diameter and outlet diameter. Increase in the inlet diameter allows more neutron throughput.

In addition, the increase in outlet opening significantly introduces more beam tail distribution than a larger inlet opening. Output quality, mentioned in equation 1, is the fraction of beam particles counted to the total neutron counted. Figure 9 shows the

output quality for both inlet and outlet simulations. As the outlet opening increases in diameter, the output quality decreases rapidly to less than 40%. However, opening the source-side inlet decreases less rapidly and was able to keep output quality above 80%.

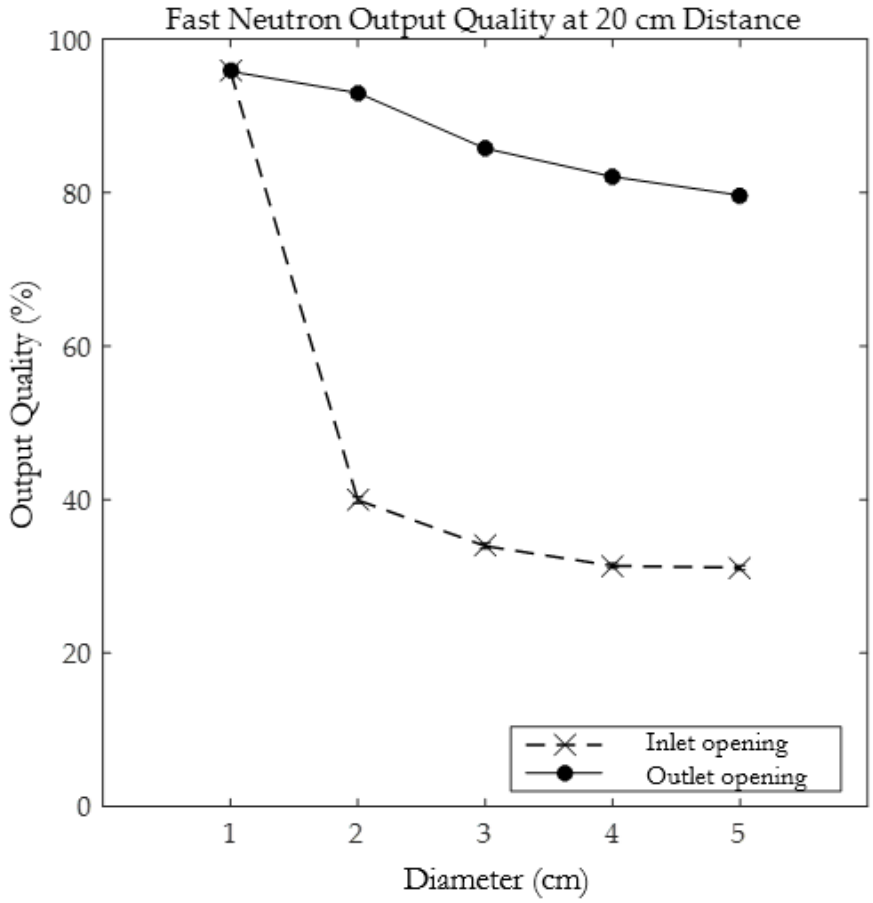

Figure 9: Comparison of neutron output quality for target-side opening and source-side opening. A tapering outlet opening resulted in a significantly lower output quality.

Upon inspection of increasing source-side or target-side openings, a tapered outlet opening diminishes the quality in collimated output without significant neutron throughput. Tapered inlet opening provided an increase in neutron throughput and a decrease in output quality. Thus, the following simulations will consider a tapering inlet bore with a narrow aperture and outlet as the optimal option.

4.2 Aperture Placement

A set of 13 simulations is compared by moving the neck of opening farther or closer to the source. The neck, or aperture placement, was located at 13, 26, or 39 cm from the source. The aperture-outlet openings are kept at 1 cm, and the inlet openings were investigated at 2, 3, 4, and 5 cm in diameter. Figure 10 displays the fast neutrons counted as the primary beam for combinations in inlet size and aperture placement. Increase in inlet size allows more neutron throughput as mentioned in the earlier section. In addition, placing the aperture further from the source will allow more neutron throughput. Due to less attenuating materials, neck placed farther from the source permits more neutron throughput.

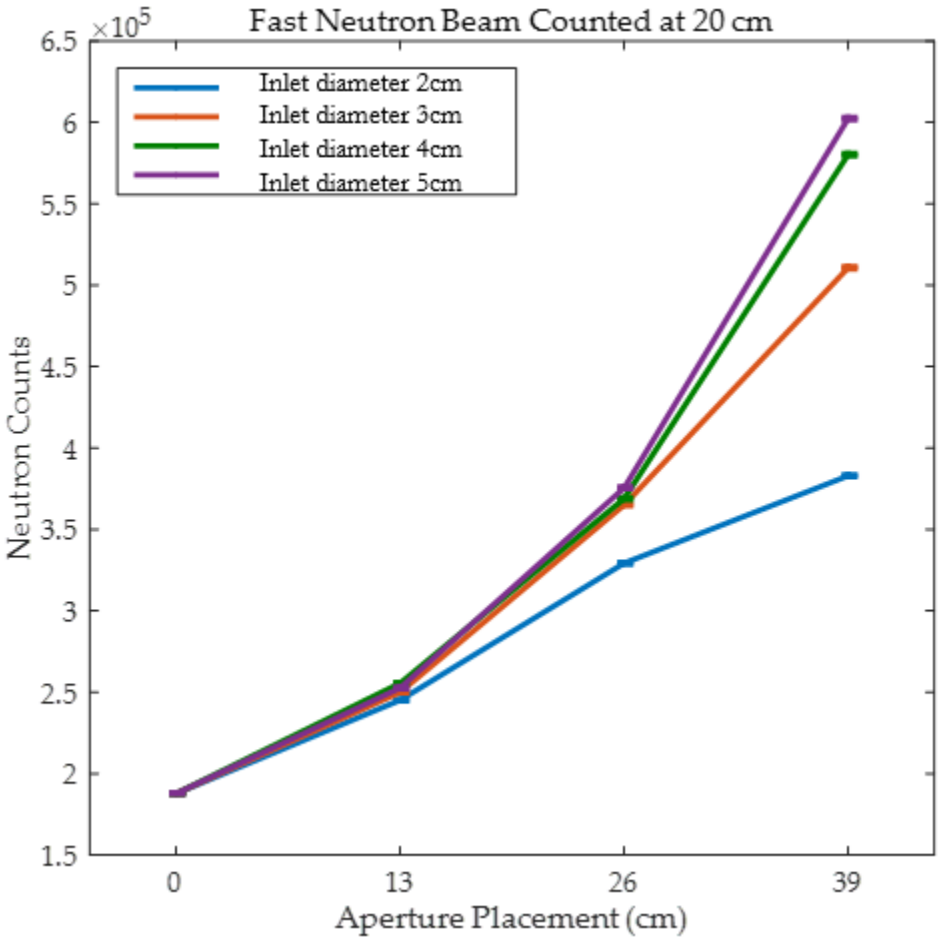

Figure 10: Comparison of neutron counts for different inlet diameters at various aperture placements. Aperture placement further from the source, 39 cm, resulted in high neutron throughput.

Although a neck placement farther from the source increases neutron throughput, the output quality must be monitored carefully. The output quality for different combinations of inlet size and neck placement is displayed in Figure 11. At 39 cm, the largest inlet opening of 5 cm resulted in the lowest output quality of about 64%. However, the smallest inlet size of 2 cm resulted in the output quality of 92%, which is

comparable to the cylindrical opening of 95%. As the neck placement moves closer to the source, the output quality curves for different inlet diameters almost converge with each other and are within a range of 91-93%.

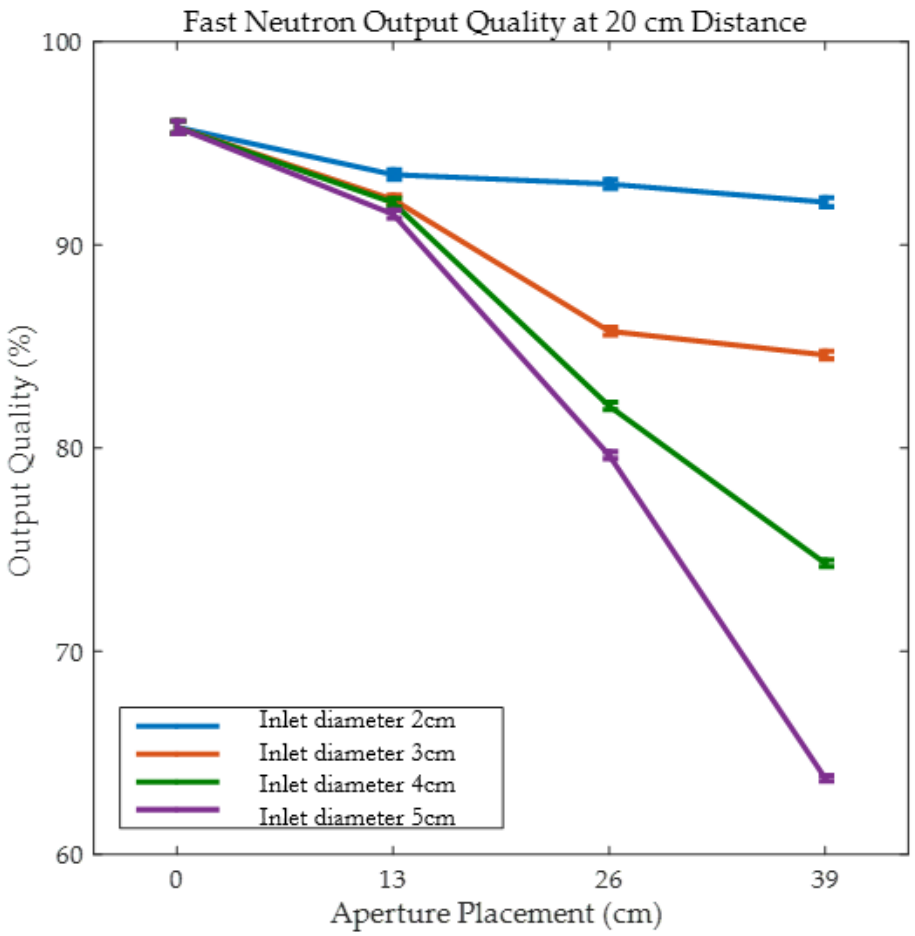

Figure 11: Comparison of fast neutron output quality for different inlet diameters at various aperture placements. Aperture placement farther from the source, 39 cm, resulted in lower output quality.

4.3 Aperture Size

Because the combinations in tapering inlet opening and distal neck placements show potential in optimizing neutron throughput and output quality, these parameters are paired with varying aperture sizes. The narrowing of the aperture would expect to improve spatial resolution by producing a smaller beam-width. A total of 65 collimator designs were simulated to inspect the beam-width. Cylindrical openings were investigated at 0.50, 0.75, 1.00, 1.25, and 1.50 cm in diameter. Similar to the previous section, the diameter of the inlet opening (2, 3, 4, and 5 cm) and neck placement (13, 26, and 39 cm) varies from the cylindrical geometry.

The simulation result shows that the FWHM of the beam is comparable to the width of the aperture. Figure 12 shows the comparison in the aperture diameter and the resulting beam-width. All simulations were categorized in the apertures sizes (0.5, 0.75, 1.0, 1.25 and 1.5 cm) and plotted with the resulting FWHM. A linear relationship is observed for the aperture size and beam width of the fast neutrons. Because the differences in FWHM and aperture size are in the magnitude of millimeters, the beam-width was assumed to be equal to the aperture size and sample spacing for NSECT imaging in the following section.

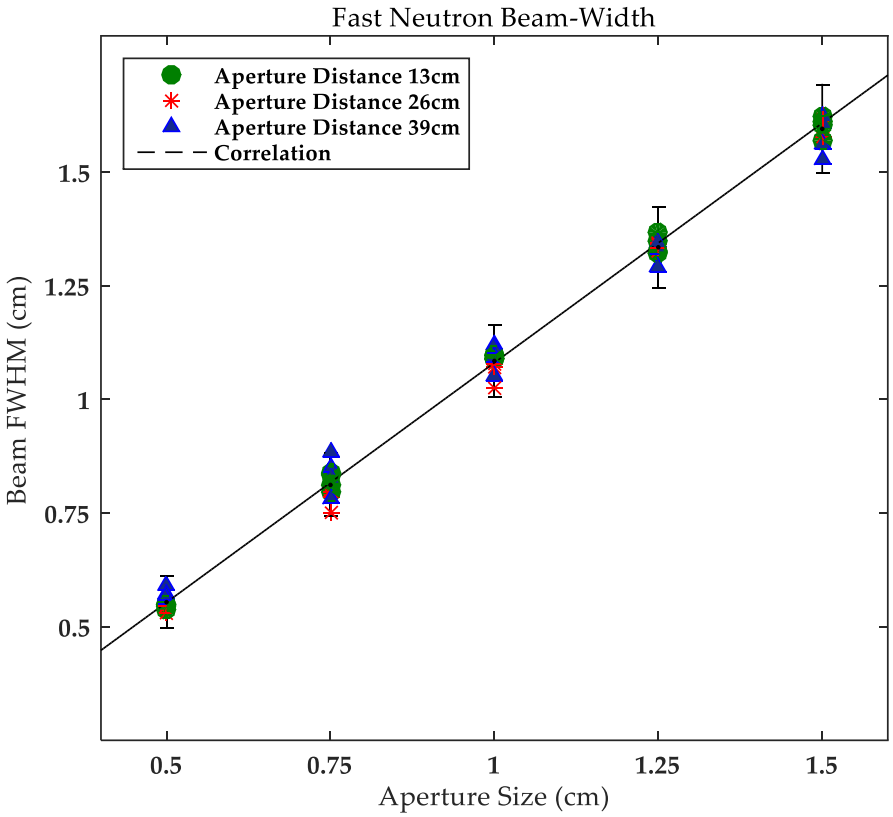

Figure 12: Beam-width of the primary neutron beam is comparable to the diameter of the aperture. Differences are in millimeters.

4.4 Collimator Design Inventory

Simulated collimator designs for DD-generators have been tested and evaluated for the purpose of NSECT imaging. Neutron fluence and output quality have been listed for 65 simulated designs in Tables 4-8. Tables 4-8 are specific to the aperture sizes of 0.5, 0.75, 1, 1.25, and 1.5 cm, respectively. The tables include results of the cylindrical designs and the taper bore inlet designs.

Listed geometries can be sorted for a preferable neutron output, based on spatial resolution, output efficiency, and noise reduction, for a specific NSECT application. Spatial resolution will be mainly influenced by the beam-width of the neutron output, which is equivalent to the aperture diameter. Differences in beam-width and aperture diameter were in the magnitude of millimeters. In addition, results of neutron fluence were calculated by assuming a 1×10^9 neutrons/s intensity Adelphi generator and using the number of neutrons detected from the 10^9 Monte Carlo histories (2-second pulse for 2π emission). Because the results were normalized to a 10^9 neutrons/s DD generator, neutron fluence can be modified to another nominal source strength of 2.5 MeV neutrons in isotropic intensity and small origin size. Lastly, the output quality is listed to provide an estimate of the fraction of fast neutrons that is the primary beam and beam tails.

Table 4: Neutron output for 0.5 cm Aperture Collimators.

Aperture Diameter (cm)	Aperture Placement (cm)	Inlet Diameter (cm)	Beam Fluence (Neutrons/sec)	Output Quality (%)
0.5	0	0.5	1.20E+04 ± 2.74E+01	95.3 ± 0.9
	13	2	1.58E+04 ± 3.15E+01	91.3 ± 0.7
		3	1.65E+04 ± 3.21E+01	91.1 ± 0.7
		4	1.64E+04 ± 3.21E+01	90.2 ± 0.7
		5	1.62E+04 ± 3.18E+01	88.8 ± 0.7
	26	2	2.39E+04 ± 3.86E+01	83.8 ± 0.5
		3	2.41E+04 ± 3.88E+01	79 ± 0.5
		4	2.47E+04 ± 3.93E+01	74.6 ± 0.5
		5	2.48E+04 ± 3.93E+01	70 ± 0.4
	39	2	3.87E+04 ± 4.92E+01	78.5 ± 0.4
		3	4.11E+04 ± 5.07E+01	59.1 ± 0.3
		4	4.23E+04 ± 5.14E+01	47.1 ± 0.2
		5	4.37E+04 ± 5.23E+01	38.4 ± 0.2

Table 5: Neutron output for 0.75 cm Aperture Collimators.

Aperture Diameter (cm)	Aperture Placement (cm)	Inlet Diameter (cm)	Beam Fluence (Neutrons/sec)	Output Quality (%)
0.75	0	0.75	3.97E+04 ± 4.98E+01	95.8 ± 0.5
	13	2	5.39E+04 ± 5.80E+01	93.6 ± 0.4
		3	5.45E+04 ± 5.84E+01	92.9 ± 0.4
		4	5.54E+04 ± 5.89E+01	92.7 ± 0.4
		5	5.49E+04 ± 5.86E+01	91.8 ± 0.4
	26	2	7.73E+04 ± 6.95E+01	90.6 ± 0.3
		3	8.04E+04 ± 7.09E+01	84.8 ± 0.3
		4	8.25E+04 ± 7.18E+01	81.4 ± 0.3
		5	8.44E+04 ± 7.26E+01	9.1 ± 0.3
	39	2	1.03E+05 ± 8.01E+01	89.4 ± 0.3
		3	1.28E+05 ± 8.96E+01	78.3 ± 0.2
		4	1.37E+05 ± 9.24E+01	64.8 ± 0.2
		5	1.41E+05 ± 9.37E+01	54.9 ± 0.1

Table 6: Neutron output for 1 cm Aperture Collimators.

Aperture Diameter (cm)	Aperture Placement (cm)	Inlet Diameter (cm)	Beam Fluence (Neutrons/sec)	Output Quality (%)
1	0	1	9.39E+04 ± 7.66E+01	95.8 ± 0.3
	13	2	1.23E+05 ± 8.75E+01	93.5 ± 0.3
		3	1.25E+05 ± 8.84E+01	92.2 ± 0.3
		4	1.28E+05 ± 8.94E+01	92.1 ± 0.3
		5	1.26E+05 ± 8.89E+01	91.5 ± 0.3
	26	2	1.65E+05 ± 1.01E+02	93.0 ± 0.2
		3	1.83E+05 ± 1.07E+02	85.8 ± 0.2
		4	1.84E+05 ± 1.07E+02	82.1 ± 0.2
		5	1.88E+05 ± 1.08E+02	79.7 ± 0.2
	39	2	1.91E+05 ± 1.09E+02	92.1 ± 0.2
		3	2.55E+05 ± 1.26E+02	84.6 ± 0.2
		4	2.90E+05 ± 1.35E+02	74.3 ± 0.1
		5	3.01E+05 ± 1.37E+02	63.8 ± 0.1

Table 7: Neutron output for 1.25 cm Aperture Collimators.

Aperture Diameter (cm)	Aperture Placement (cm)	Inlet Diameter (cm)	Beam Fluence (Neutrons/sec)	Output Quality (%)
1.25	0	1.25	1.84E+05 ± 1.07E+02	95.6 ± 0.2
	13	2	2.36E+05 ± 1.21E+02	94.6 ± 0.2
		3	2.45E+05 ± 1.24E+02	93.2 ± 0.2
		4	2.48E+05 ± 1.25E+02	92.5 ± 0.2
		5	2.48E+05 ± 1.24E+02	92.1 ± 0.2
	26	2	2.82E+05 ± 1.33E+02	94.4 ± 0.2
		3	3.46E+05 ± 1.47E+02	90.7 ± 0.2
		4	3.61E+05 ± 1.50E+02	85.3 ± 0.1
		5	3.66E+05 ± 1.51E+02	82.6 ± 0.1
	39	2	3.05E+05 ± 1.38E+02	93.9 ± 0.2
		3	4.33E+05 ± 1.64E+02	89.6 ± 0.1
		4	5.22E+05 ± 1.81E+02	83.3 ± 0.1
		5	5.71E+05 ± 1.89E+02	75.2 ± 0.1

Table 8: Neutron output for 1.5 cm Aperture Collimators.

Aperture Diameter (cm)	Aperture Placement (cm)	Inlet Diameter (cm)	Beam Fluence (Neutrons/sec)	Output Quality (%)
1.5	0	1.5	3.17E+05 ± 1.41E+02	95.4 ± 0.2
	13	2	3.84E+05 ± 1.55E+02	94.8 ± 0.2
		3	4.18E+05 ± 1.62E+02	93.1 ± 0.1
		4	4.25E+05 ± 1.63E+02	92.3 ± 0.1
		5	4.28E+05 ± 1.64E+02	91.8 ± 0.1
	26	2	4.23E+05 ± 1.63E+02	94.8 ± 0.1
		3	5.51E+05 ± 1.85E+02	92.0 ± 0.1
		4	6.02E+05 ± 1.94E+02	87.1 ± 0.1
		5	6.12E+05 ± 1.96E+02	83.3 ± 0.1
	39	2	4.40E+05 ± 1.66E+02	94.5 ± 0.1
		3	6.40E+05 ± 2.00E+02	91.2 ± 0.1
		4	7.92E+05 ± 2.23E+02	86.1 ± 0.1
		5	8.98E+05 ± 2.37E+02	80.2 ± 0.1

5. NSECT Imaging

The series of simulated collimator designs were investigated for the purpose of a clinical NSECT system. Their collimated beams were evaluated in neutron flux, beam-width, and output quality. To assess these collimator qualities and demonstrate their performance in an imaging application, an anthropomorphic female phantom was implanted with a breast tumor lesion and scanned using NSECT. Tomographic geometry consisted of 8 rotation increments from 0 to 180 degrees, which is consistent with NSECT dose studies performed previously in our group (Belley et al. 2014). Unlike the previous study, this scan was performed to analyze image quality rather than dose. To fully understand the images obtained from different DD neutron collimators, the neutron flux was based on a 10 second scan for each translation step. The scan time would be the same for images of the same tomographic geometry. Neutron throughput would depend on the collimator used. After scanning the phantom, images were reconstructed using characteristic gamma rays from bromine. The bromine concentration is about 7.3% lower in malignant breast tissue than healthy breast tissue. Previous studies have shown that NSECT was able to differentiate healthy breast tissues from malignant breast tissues for bromine concentration (Bender et al. 2007).

Table 9 shows the differences in the collimator designs and outputs. Collimators were chosen for output qualities of 95%, 90%, 79%, 70%, and 59% while having the beam-width of 0.5 cm. All cylindrical openings of a given aperture size showed the

greatest output quality of about 95%. In comparison, the tapering designs showed output quality values of about 60% to 90%. The finest aperture size of 0.5 cm was chosen for all geometries. Results of bromine concentration were calculated for a filtered back-projection image because the pixel intensities would have a more accurate representation of elemental concentration prior to the iterative processing of MLEM. The average pixel intensity was approximated with a 2.5 cm diameter region of interest around the lesion location. This lesion pixel intensity was compared to the surrounding healthy tissues. From this acquisition, images acquired with output qualities of 79% and greater resulted in a bromine contrast larger than the actual bromine difference of 7.3%. The 70% and 59% output qualities resulted in less than 7.3% bromine difference. It was expected that a lower output quality would result in a lower bromine contrast in the image due to higher background neutrons.

Table 9: Bromine differences from collimators of varying output qualities.

Aperture Diameter (cm)	Inlet Diameter (cm)	Neck Distance (cm)	Output Quality (%)	Bromine Difference (%)
0.5	**0.5**	**-**	**95**	8.5
0.5	**4**	**13**	**90**	9.3
0.5	**3**	**26**	**79**	9.0
0.5	**5**	**26**	**70**	6.0
0.5	**3**	**39**	**59**	6.9

After noting the elemental differences, the images were subject to ML-EM for 40 iterations. These images are depicted in Figure 13, where a depression of bromine concentration can be seen near the right of the breast slice. This bromine depression, where the lesion is located, is evident in all images. However, the healthy tissue area also shows depressions and heterogeneities in concentration, especially in images acquired from greater output qualities. Although the collimator of 59% had the lowest output quality, the normal breast tissues are more homogenous in concentration. The tapering collimator of 59% (used for image (e)) allowed about a three-fold greater neutron flux than the cylindrical collimator of 95% (used for image (a)). As the output quality decreases and flux increases, the images become sharper due to the increase in signal. These results show the benefit in tapering collimator designs for the goal of optimizing neutron throughput.

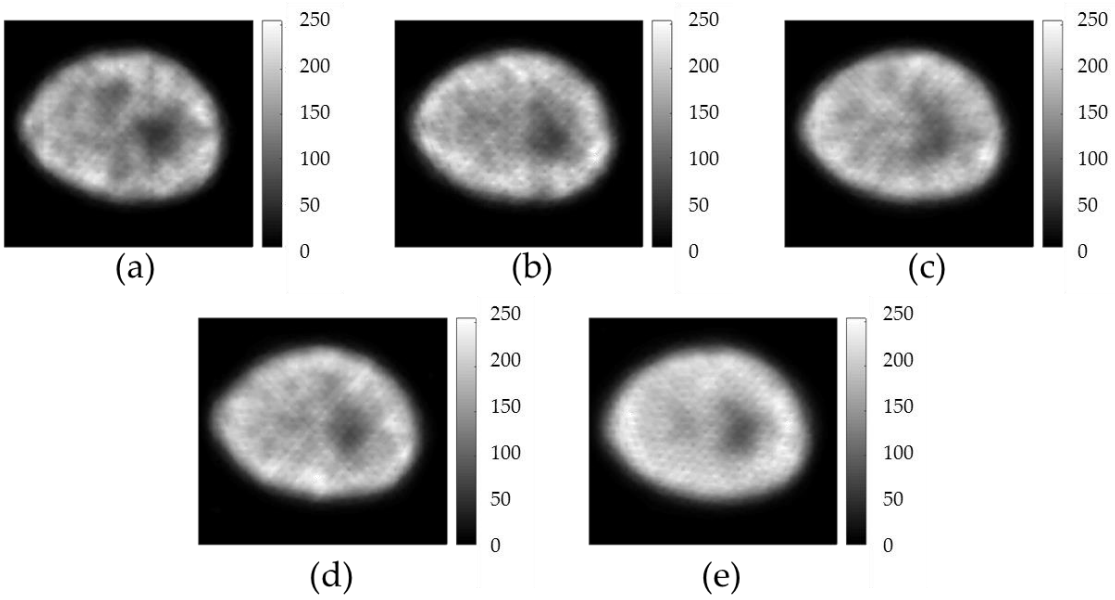

Figure 13: Subplots (a-e) are NSECT breast scans in the order of decreasing output qualities: 95%, 90%, 79%, 70%, and 59%. Images show bromine concentration in a breast lesion surrounded by healthy tissue.

Secondly, the feature of aperture diameter was assessed through simulated breast scans. From the collimator simulations, the resulting beam-width was found to be comparable to the diameter of the physical aperture. These dimensions of beam-width were used for the sample-spacing distance in tomographic imaging, where translations of the collimated beam are in increments equal to the beam-width. Since the translation distance determines how fine NSECT can scan the breast, the beam-width is a major factor in the resulting spatial resolution in the image. To depict the influence of the beam-width on resolution, breast scans were performed with collimators listed in Table 10. Aperture diameters ranged from 0.5 to 1.5 cm with the same output quality of 95%.

The breast lesion in the images, acquired using the listed collimators, were compared with the actual lesion size of about 2.5 cm. Line profiles were taken across the images to calculate the simulated lesion FWHM. All images underestimated the actual lesion size where the larger apertures (1.25 and 1.5 cm) resulted in lesion sizes 0.5 and 0.6 cm smaller.

Table 10: Bromine differences from collimators of varying aperture diameters.

Aperture Diameter (cm)	Inlet Diameter (cm)	Neck Distance (cm)	Output Quality (%)	Lesion FWHM (cm)
0.5	**0.5**	**-**	**95**	2.3
0.75	**0.75**	**-**	**95**	2.2
1.0	**1.0**	**-**	**95**	2.4
1.25	**1.25**	**-**	**95**	1.9
1.5	**1.5**	**-**	**95**	2.0

Figure 14 shows the images acquired from the different aperture sizes. Although the line profiles were able to detect bromine depression where the lesion was expected to be, images from the larger apertures were more difficult to identify. The noisy appearance in healthy tissue was more dramatic as the aperture size increased. The pronounced patterned noise appearance results from the low sampling rate and ML-EM algorithm. Depression from the actual lesion is obscured from the pattern. For practical

usage in tomographic imaging of small lesions, a smaller aperture size would be beneficial to identify lesions of unknown locations.

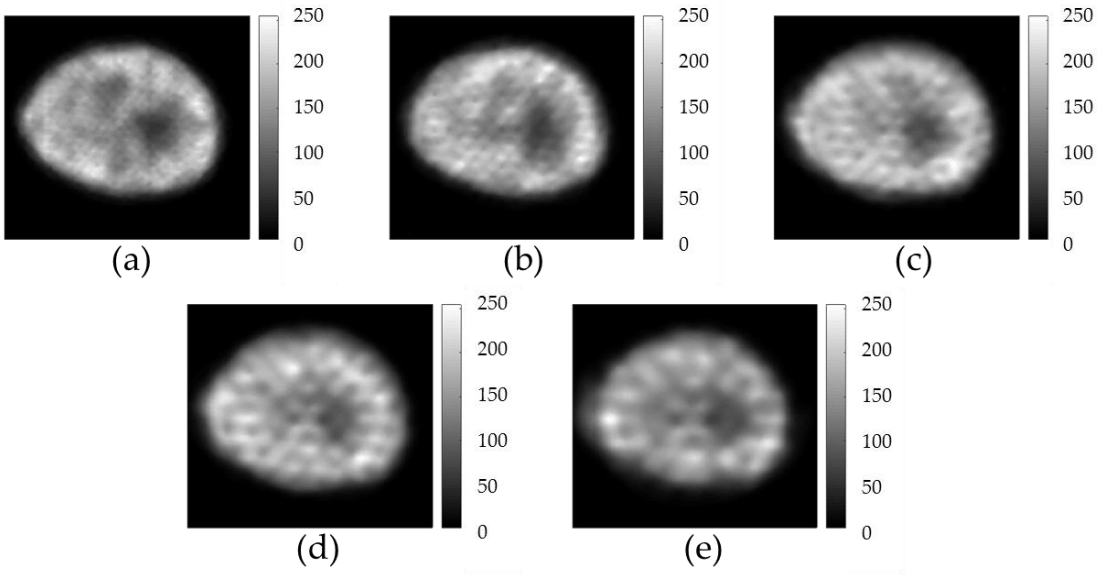

Figure 14: Subplots (a-e) are NSECT breast scans in the order of increasing aperture diameter: 0.5, 0.75, 1.0, 1.25, and 1.5 cm. Images show bromine concentration in a breast lesion surrounded by healthy tissue.

6. Conclusion and Future Plans

The results of this work demonstrate the ability to collimate a DD neutron generator output to produce a neutron beam suitable for NSECT imaging. To implement DD generators into a real clinical system, the collimator must be chosen carefully for the purpose of imaging. Measures of neutron flux, output quality, and beam-width should be considered and have been cataloged for future NSECT reference.

A tapering collimator design has shown potential advantages over the cylindrical opening. By tapering the inlet and placing the aperture farther from the source, the collimator increases neutron throughput. This increase in throughput, which results in higher neutron flux at the target, allows for faster scans and greater efficiency in generator usage. Although tapering designs are favorable for high flux, these designs sacrifice output quality, which may be as low as 40%. Cylindrical designs have the highest output quality of approximately 95% regardless of aperture size. Thus, cylindrical designs might be necessary to optimally lower the noise and dose in a clinical NSECT scan. These qualities should be taken into consideration when choosing a collimator design for a particular NSECT application.

In summary, this work has demonstrated the potential of implementing a DD neutron generator for use in a clinical NSECT system. The proposed collimator designs can produce collimated neutron beams capable of breast imaging with millimeter resolution. The next step for our research group is to continue on the development of

NSECT into the new clinical system. After the collimator and source have been investigated, we will investigate proper shielding that would encase all components of system (including the target, source, collimator, and detectors) and protect the general public from escaping radiation. This shield enclosure would allow the system to be placed in the hospital setting to perform NSECT imaging.

References

Agasthya GA, Shah JP, Harrawood BC, Kapadia AJ. *Neutron time-of-flight spectroscopy for depth-resolved quantification through NSECT.* Phys. Med. Biol 57 3034-3037, 2011

Agostinelli S et al. *Geant4--a simulation toolkit*. Nucl. Instrum. Methods Research Section A: Accelerators, Spectrometers, Detectors and Associated Equipment 506 250–303, 2003

Barton JP *Divergent Beam Collimator for Neutron Radiography.* Mater. Eval. 25 45A-46A, 1967

Bender JE, Kapadia AJ, Sharma AC, Tourassi GD, Harrawood BP, Floyd CE. *Breast cancer detection using neutron stimulated emission computed tomography: Prominent elements and dose requirements.* Med. Phys. 34 3866–3871, 2007

Belley MD, Segars WP, Kapadia AJ. *Assessment of individual organ doses in a realistic human phantom from neutron and gamma stimulated spectroscopy of the breast and liver.* Med. Phys. 41 063902, 2014

Bergaoui K, Reguigui N, Gary CK, Cremer JT, Vainionpaa JH, Piestrup MA. *Design, testing and optimization of a neutron radiography system based on a Deuterium–Deuterium (D–D) neutron generator.* Journal of Radioanalytical and Nuclear Chemistry 299 41-51, 2013

Floyd CE Jr, Howell C, Harrawood BP, Crowell A, Kapadia AK, Macri R, Xia J, Pedroni R, Bowsher JE, Kiser M, Tourassia GD, Tornow W, Walter R. *Neutron stimulated emission computed tomography of stable isotopes.* Proc. SPIE 5368 248–254, 2004

Floyd CE Jr, Bender JE, Sharma AC, Kapadia AJ, Xia J, Harrawood BP, Tourassi GD, Lo JY, Crowell A, Howell CR. *Introduction to neutron stimulated emission computed tomography.* Phys. Med. Biol. 51 3375-3390, 2006

Floyd CE Jr, Kapadia AJ, Bender JE, Sharma AC, Xia QX, Harrawood BP, Tourassi GD, Lo JY, Crowell AS, Kiser MR, Howell CR. *Neutron-stimulated emission computed tomography of a multi-element phantom.* Phys. Med. Biol. 53 2313-2326, 2008

Harrawood BP, Agasthya GA, Lakshmanan MN, Raterman G, Kapadia AJ. *Geant4 distributed computing for compact clusters.* Nucl Instr Meth Phys Res A. 764 11-17, 2014

Kapadia AJ, Sharma AC, Bender JE, Tourassi GD, Howell CR, Crowell AS, Kiser MR, Harrawood BP, Floyd CE. *Neutron stimulated emission computed tomography for diagnosis of breast cancer.* IEEE Trans. Nucl. Sci. 55 501–509, 2008a

Kapadia AJ, Tourassi GD, Sharma AC, Crowell AS, Kiser MR and Howell CR. *Experimental detection of iron overload in liver through neutron stimulated emission spectroscopy.* Phys. Med. Biol. 53 2633-2649, 2008b

Kapadia A, Crowell A, Fallin B, Howell C, Agasthya G, Lakshmanan M, Newton J, Juang T, Oldham M. *Measurement of Neutron Dose from a Novel Neutron Imaging Technique.* Medical Physics 39 3727-3727, 2014

Lakshmanan MN, Kapadia AJ. 2012 *Quantitative assessment of lesion detection accuracy, resolution, and reconstruction algorithms in neutron stimulated emission computed tomography*. IEEE Trans Med Imag. 31 1426-1435, 2012

Lakshmanan MN, Harrawood BP, Rusev G, Agasthya GA, Kapadia AJ. *Simulations of nuclear resonance fluorescence in Geant4.* Nucl Instr Meth Phys Res A. 763 89-96, 2014

Segars WP, Sturgeon G, Mendonca S, Grimes J, Tsui BMW. *4D XCAT phantom for multimodality imaging research*. Med. Phys. 37 4902, 2010

Solomon J, Nelson R, Samei E. *Tu-c-103-01: A framework for 3d modeling of anthropomorphic lesions in ct.* Med. Phys. 40 436–436, 2013

Solomon J, Samei E. *A generic framework to simulate realistic lung, liver and renal pathologies in ct imaging*. Phys. Med. Biol. 59 6637, 2014

Sharma AC, Harrawood BP, Kapadia AJ, Bender JE, and Tourassi GD. *Neutron stimulated emission computed tomography: A Monte Carlo simulation approach.* Phys. Med. Biol. 52 6117–6131, 2007

Viana RS, Agasthya GA, Yoriyaz H, Kapadia AJ. *3D element imaging using NSECT for the detection of renal cancer: a simulation study in MCNP.* Phys. Med. Biol. 58 5867-5883, 2013